

SIMULTANEOUS OBSERVATIONS OF VARIABILITY AT ALL ATMOSPHERIC LEVELS OF V824 ARAE (HD 155555)¹

ROBERT C. DEMPSEY²

Astronomy Programs, Computer Sciences Corporation, Space Telescope Science Institute, 3700 San Martin Drive, Baltimore, MD 21218;
robert.c.dempsey1@jsc.nasa.gov

JAMES E. NEFF

Department of Physics and Astronomy, College of Charleston, 66 George Street, Charleston, SC 29424; neffj@cofc.edu

AND

JEREMY LIM

Institute of Astronomy and Astrophysics, Academia Sinica, P.O. Box 1-87, Nankang, Taipei, Taiwan 115; jlim@biaa.sinica.edu.tw

Received 2000 August 4; 2001 March 23

ABSTRACT

We conducted a multiwavelength campaign observing V824 Ara (HD 155555, G5 IV + K0 IV–V) continuously throughout one complete orbital cycle (~ 1.7 days) in early May of 1996. At the core of this campaign were observations using the GHRS on the *Hubble Space Telescope* (*HST*). In all, about 48,000 spectra, many in rapid readout mode, were obtained with the GHRS covering the C IV, Mg II, and Fe XXI wavelength regions at 11–15 separate phases. Simultaneous observations were made with the *Extreme Ultraviolet Explorer* (*EUVE*). Radio observations (3.5 and 6 cm) were conducted at the Australian Telescope, while ground-based visual spectroscopic and photometric observations were made at European Southern Observatory, Cerro Tololo Inter-American Observatory, the Anglo-Australian Telescope, and South African Astronomical Observatory. Additional ground-based observations were obtained before, during, and after the campaign. Our primary intent was to obtain a three-dimensional model of the atmosphere extending from the photosphere to the corona. Variability was clearly detected, including several flares observed in the *HST*, *EUVE*, and radio data. We present results from modeling the ultraviolet transition region lines using an anisotropic macroturbulence model. Previous studies of transition region lines in late-type active stars have used multiple Gaussians to fit the observed line profiles, adding broad components to account for the extended wings observed in several active systems, including V711 Tau (HR 1099). This broad component has been interpreted as arising from the continuous presence of microflaring. We demonstrate that anisotropic macroturbulence models can also explain the observed Mg II profiles.

Key words: stars: activity — stars: chromospheres — stars: coronae — stars: individual (V824 Arae) — stars: late-type

1. INTRODUCTION

Magnetic fields thread and connect the atmospheric layers of late-type stars. The strength and surface coverage of these fields is enhanced by rapid rotation, due either to youth or to spin-orbit coupling in close binary systems. Magnetic activity can form structure that is stable over many stellar rotations, but it can also lead to rapid variability. Magnetic fields permit nonradiative energy exchange between atmospheric levels and can serve as an energy storage and release mechanism. To unravel all these effects, magnetically active stars must be observed simultaneously at all atmospheric levels and continuously over two or more complete cycles.

A great deal of progress has been made in recent years in decomposing the two-dimensional structure in the atmospheres of late-type stars. Doppler images of many photospheres—rapidly rotating single stars, T Tauri stars,

Algols, and RS CVn binaries—are regularly published. Doppler images of the photosphere of the primary component of V824 Ara presented by Hatzes & Kürster (1999) reveal a large, somewhat off-center polar spot and possibly one smaller equatorial spot. Such large polar spots are common within the active post-main-sequence binaries of the RS CVn type (e.g., Vogt et al. 1999; Strassmeier et al. 1991). They have also been seen on pre-main-sequence objects (e.g., Joncour, Bertout, Bouvier 1994; Rice & Strassmeier 1996), on some zero-age main-sequence stars, such as AB Dor (Collier-Cameron 1995), and on the single Pleiades-age G2 dwarf star HD 129333 (Strassmeier & Rice 1998). Zeeman Doppler images of photospheric magnetic field structure are now feasible (Donati et al. 1992).

Spectral images of chromospheres are more difficult to derive, because less is known a priori about stellar outer atmospheres and because the observations are more difficult to obtain. Walter et al. (1987) and Neff et al. (1989) used ultraviolet spectra obtained with the *IUE* spacecraft to image the chromospheric structure of the RS CVn binary system AR Lac. Recent studies based on ultraviolet spectra obtained with the *Hubble Space Telescope* (*HST*) have shown that many active stars possess complex chromospheric and transition region line profiles. In 1993 we observed the RS CVn binary V711 Tau at several phases

¹ Based on observations with the NASA/ESA *Hubble Space Telescope*, obtained at the Space Telescope Science Institute, which is operated by the Association of Universities for Research in Astronomy, Inc., under NASA contract NAS 5-26555.

² Current address: Johnson Space Center, NASA Road 1, Mail Stop DF25, Houston, TX 77058.

with the GHRS in several ultraviolet bandpasses to study profile variations as a function of phase (Dempsey et al. 1996). Unfortunately, scheduling problems, pointing errors, continuous flaring, and the sparse and uneven phase sampling prevented us from achieving the primary goal. However, it is clear that several ultraviolet lines in the system, notably C IV, Si IV, and Mg II, show very extended emission-line wings out to several hundred kilometers per second. The profile shapes vary, and some of these variations are phase-dependent. Dempsey et al. (1996) and Wood, Linsky, & Ayres (1997) show that simple multi-Gaussian fits are not adequate to describe the higher quality line profiles. Vilhu et al. (1998) observed the rapidly rotating single star AB Dor continuously for 14 hr with *HST*. They find extended, non-Gaussian emission in the C IV doublet.

Following up on our study of V711 Tau, we have observed another close binary system with complete phase coverage in three key wavelength bandpasses, utilizing the ability of *HST* to observe some stars at high declinations with uninterrupted coverage (the continuous viewing zone). Generally classified as an RS CVn, V824 Ara (HD 155555) consists of a G5 IV star in a short-period orbit ($P \sim 1.68$ days) with a K0 V–IV companion (Strassmeier et al. 1993). The system does not eclipse, but both stellar components rotate rapidly ($v \sin i = 37$ and 29 km s^{-1} for the G and K star components, respectively). There is also an M star visual companion (LDS 587B) $33''$ away. The space velocities of the stars suggests that the binary is part of the young disk population, which agrees with the high Li I $\lambda 6708$ abundance (Pasquini et al. 1991). With the M star companion showing very high levels of activity, it seems likely that the V824 Ara + LDS 587B system is pre-main sequence. Photometric observations by Cutispoto (1993) show an amplitude $\Delta V \approx 0.12$ with a photometric (rotational) period equal to the orbital period derived by Pasquini et al. (1991). Dempsey et al. (1993a) measured a ROSAT PSPC X-ray luminosity of $2.74 \times 10^{30} \text{ ergs s}^{-1}$. Two-temperature coronal models were applied to the PSPC X-ray pulse-height spectra by Dempsey et al. (1993b). They find that the lower temperature component is consistent with the full sample of RS CVn binaries studied, but the hot component is slightly lower than the sample as a whole. Moderate Ca II H and K emission, “filled-in” H α , and radio emission are also consistent with this being a fairly active, short-period binary system (Strassmeier et al. 1993).

Preliminary results from this campaign were presented by Dempsey et al. (1998). In this paper we concentrate on the analysis of the simultaneous ultraviolet, extreme ultraviolet, and radio observations. More detailed studies of the phase dependence of the visible and ultraviolet line profiles, and therefore of the photospheric and chromospheric structure, will be published separately.

2. OBSERVATIONS

In 1996 May we conducted a campaign of multi-wavelength observations of V824 Ara. We used the *HST* GHRS simultaneously with the *Extreme Ultraviolet Explorer* (*EUVE*) spacecraft and with ground-based radio and visual observations. We are therefore able to compare the atmospheric variability and structure at all levels, from the photosphere through the corona (Neff et al. 1996). In this paper, we present the ultraviolet, extreme ultraviolet, and radio results, paying particular attention to the simul-

taneous observations. The visual photometry and spectroscopy were obtained for several weeks before, during, and after the campaign. These data will be used here only to define the context of the campaign. They will be used in other papers to derive detailed images of the photospheric surface structure.

To discriminate between time-variable and phase-dependent effects, we report our results in terms of the fractional number of 1.681652 day orbits (and rotations) of V824 Ara since the epoch HJD = 2,446,998.4102 (Pasquini et al. 1991). $\Phi = 0.25$ corresponds to conjunction with the K star “in front” of the G star from our perspective.

2.1. GHRS Observations

The ultraviolet spectral region covered by the Goddard High Resolution Spectrograph (GHRS) on *HST* includes emission lines arising from stellar chromospheres and transition regions. The Fe XXI line at 1354.14 \AA serves as a diagnostic of stellar coronae. Observations with the GHRS were obtained when V824 Ara was in the continuous viewing zone. The target was continuously in view for approximately nine *HST* orbits, each 96 minutes long, before the South Atlantic Anomaly (SAA) was crossed. During passage through the SAA, the GHRS was paused because of the high radiation. For the next several orbits the SAA was crossed briefly, followed again by nine orbits of SAA-free observing. Observations were scheduled to cycle between the C IV, Mg II, and Fe XXI regions. To optimize observing efficiency, this order was not always maintained if insufficient observing time was available to perform a full integration. Single observations at other wavelengths were obtained to ascertain global atmospheric properties (e.g., emission measures) when small windows, too short for a full observation of one of the three key bandpasses, occurred in the schedule. In this manner observations of key chromospheric and transition-region lines such as O I, Si II, Si III], C III], Si IV, O IV, and He II were obtained. No information about variability of these lines was obtained. Our observing log is presented in Table 1. Because of a scheduling error at the STScI, the last two orbits of scheduled observing time were lost.

All observations were obtained with side 2 of the GHRS and the G160M grating, except for the Mg II data, which used the echelle B grating (ECH-B). The Fe XXI spectra were read out using the RAPID mode of the GHRS (except for one ACCUM observation, Z364030LT) so that good time resolution would be available in the event of a flare. In this mode the detector is read out in 1 s intervals. To reduce overhead, no quarter stepping was performed, so there was virtually no dead time between readouts, but detector granularity is retained in the data and spectral resolution is reduced slightly (1 diode $\approx 16 \text{ km s}^{-1}$). All other spectra were obtained in FP-SPLIT ACCUM mode with quarter stepping. Spectral resolution was approximately 3.5 km s^{-1} diode $^{-1}$ for the G160M and 0.8 km s^{-1} diode $^{-1}$ for the ECH-B. Since orbital motion could be significant, thereby causing phase smearing of the line profiles, we observed with the large science aperture (LSA) to maximize throughput and keep exposure times as short as possible. To prevent the possible loss of significant amounts of data in the event of an instrument problem (e.g., grating carousel reset), the RAPID readout observations were broken up into paired exposures. One observation (Z364040QT) had a minor degradation of data caused by a brief loss of guide-

TABLE 1
SUMMARY OF GHRS OBSERVATIONS

Observation	Wavelength Region	HJD at Start	Orbital Phase ^a	Exposure (s)
Z3640109T	C IV	2,450,203.5505	1905.9474	1523.2
Z364010CT	Mg II	2,450,203.5703	1905.9592	761.6
Z364010GT	Fe XXI	2,450,203.5974	1905.9753	2259.2
Z364010IT	Fe XXI	2,450,203.6260	1905.9923	2232.2
Z364010LT	C IV	2,450,203.6550	1906.0096	1523.2
Z364010OT	Mg II	2,450,203.6754	1906.0217	761.6
Z364010ST	Fe XXI	2,450,203.7017	1906.0373	2250.2
Z364010UT	Fe XXI	2,450,203.7300	1906.0542	2263.2
Z364010WT	He II	2,450,203.7552	1906.0692	1523.2
Z3640207T	C IV	2,450,203.8102	1906.1018	1523.2
Z364020AT	Mg II	2,450,203.8300	1906.1136	761.6
Z364020ET	Fe XXI	2,450,203.8560	1906.1291	2264.2
Z364020GT	Fe XXI	2,450,203.8845	1906.1460	2249.2
Z364020JT	C IV	2,450,203.9131	1906.1630	1523.2
Z364020MT	Fe XXI	2,450,203.9412	1906.1798	2263.2
Z364020OT	Fe XXI	2,450,203.9697	1906.1967	2256.2
Z364020RT	Mg II	2,450,203.9995	1906.2144	761.6
Z364020TT	Si III], C III]	2,450,204.0200	1906.2266	1196.8
Z3640306T	Mg II	2,450,204.0558	1906.2479	544.0
Z364030AT	Fe XXI	2,450,204.0929	1906.2700	2054.2
Z364030CT	Fe XXI	2,450,204.1190	1906.2855	2053.2
Z364030FT	C IV	2,450,204.1666	1906.3138	1849.6
Z364030IT	Mg II	2,450,204.1887	1906.3269	1088.0
Z364030LT	Fe XXI ^b	2,450,204.2299	1906.3514	3699.2
Z364030NM	C IV	2,450,204.2803	1906.3814	1414.4
Z364030QT	Mg II	2,450,204.3062	1906.3968	761.6
Z364030ST	Si IV, O IV	2,450,204.3156	1906.4024	435.2
Z3640407T	C IV	2,450,204.3814	1906.4415	1523.2
Z364040AT	Mg II	2,450,204.4012	1906.4533	761.6
Z364040ET	Fe XXI	2,450,204.4428	1906.4781	2265.2
Z364040GT	Fe XXI	2,450,204.4713	1906.4950	2264.2
Z364040JT	C IV	2,450,204.5000	1906.5121	1523.2
Z364040MT	Mg II	2,450,204.5197	1906.5238	761.6
Z364040QT	Fe XXI	2,450,204.5459	1906.5394	2201.2
Z364040ST	Fe XXI	2,450,204.5743	1906.5563	2248.2
Z364040UT	O I	2,450,204.5996	1906.5713	1523.2
Z3640507T	C IV	2,450,204.6500	1906.6013	1523.2
Z364050AT	Mg II	2,450,204.6699	1906.6131	761.6
Z364050ET	Fe XXI	2,450,204.6959	1906.6285	2256.2
Z364050GT	Fe XXI	2,450,204.7247	1906.6456	2205.2
Z364050JT	C IV	2,450,204.7530	1906.6625	1523.2
Z364050MT	Mg II	2,450,204.7729	1906.6743	761.6
Z364050QT	Fe XXI	2,450,204.7998	1906.6903	2248.2
Z364050ST	Fe XXI	2,450,204.8282	1906.7072	2247.2
Z364050VT	Mg II	2,450,204.8525	1906.7216	761.6
Z3640606T	Mg II	2,450,204.8867	1906.7420	544.0
Z364060AT	Fe XXI	2,450,204.9099	1906.7558	2053.2
Z364060CT	Fe XXI	2,450,204.9361	1906.7714	2034.2
Z364060FT	C IV	2,450,204.9653	1906.7888	1849.6
Z364060IT	Mg II	2,450,204.9890	1906.8028	1088.0
Z364060MT	Fe XXI	2,450,205.0314	1906.8281	2048.2
Z364060OT	Fe XXI	2,450,205.0458	1906.8367	2035.2
Z364060RT	C IV	2,450,205.0993	1906.8684	1414.4
Z364060UT	Mg II	2,450,205.1185	1906.8798	761.6
Z364060WT	Si II	2,450,205.1299	1906.8866	544.0

^a Phases calculated from $\Phi = \text{HJD } 2,446,998.4102 + 1.681652E$ (Pasquini et al. 1991).

^b ACCUM mode, all other Fe XXI spectra are RAPID.

star fine lock. Affected readouts of this exposure were not used.

Whenever possible, wavelength calibration spectra were obtained prior to the start of each observation. The GHRS SPYBAL positioning observation (Soderblom, Sherbert, &

Hulbert 1993) was used if no other wavelength calibration was available. Previous studies have found that the default wavelength calibration is accurate to better than 1 km s^{-1} for the first-order gratings and 0.6 km s^{-1} for the echelle B grating. Using the calibration spectra taken at the time of

the science observation improves the accuracy to approximately 0.1 km s^{-1} . Using the SPYBAL spectrum yields an accuracy somewhere between the default calibration and that obtained with a contemporaneous comparison observation. All observations were calibrated in standard fashion using the GHRS Data Analysis Facility software, 1993 December version (Blackwell et al. 1993). This calibration also includes correction for geomagnetic induced motion perturbation, which can induce velocity shifts over long exposures. Vignetting and flux calibration used the Robinson et al. (1996) values and are accurate to about 10%.

In Figures 1 and 2 we show all the Mg II and C IV spectra. Spectra obtained at other wavelengths are displayed in Figure 3. The lone ACCUM spectrum of the Fe XXI wavelength region is shown in Figure 4, with several key features indicated.

During the entire observing campaign 48,313 spectra were obtained once per second in RAPID readout mode. Observing in this mode is a trade-off: high time resolution is obtained at the expense of spectral resolution, because quarter stepping of the grating is not performed. Maran et al. (1994) presented a detailed analysis of a large number of RAPID readouts of AU Mic, which we followed with some small changes. Since binary orbital motion is significant in the V824 Ara system, we cannot sum all the spectra together. Furthermore, the count rate was lower than for AU Mic.

In addition to known turned-off diodes (Heap et al. 1995), it has recently become apparent that there are “flaky” diodes (Schultz & Bacinski 1996). These diodes are normal most of the time but occasionally do not register fully, because of thermally induced nonlinear amplification effects in the detector pre-amp. Careful analysis of diode behavior in conjunction with instrument temperature suggests that the effect might increase as the instrument warms up, but no definitive correlation has yet been determined. Short observations tend not to experience this effect, but our observations were obtained in the continuous viewing zone, where solar heating of the aft shroud can be significant. While preparing for the second servicing mission, the GHRS observations were obtained with the Faint Object Spectrograph electronics turned on to ascertain how the new instruments might affect the aft shroud temperature. With high signal-to-noise spectra it can be easy to identify their location and when they are not registering properly. However, with the low count rate observed for V824 Ara, this was not possible.

Several “hot” diodes, channels that always register the maximum value of 4096, had to be accounted for. The dead, hot, and intermittent diodes can easily be identified as sharp spikes above or below the “continuum.” As a conservative strategy, because none of these diodes were near a key emission feature, we treated them as dead diodes. For each readout, these diodes were set to the average value of adjacent diodes. Before final calibration and co-addition the data were cleaned of noisy readouts. Since the count rate in each 1 s scan was low, random noise or cosmic rays can introduce a significant number of erroneous counts. Background counts cannot be directly measured in RAPID readout mode. A delicate balance needs to be obtained in rejecting noisy readouts while not compromising real data. Maran et al. (1994) calculated the total counts in each readout. If that number exceeded a cutoff value, the scan was rejected from the final spectrum. The cutoff was deter-

mined from an estimate of the stellar flux compared with the background level. The argument is that if the counts are above the cutoff they are probably noise, and significant stellar signal is not lost if only a few readouts are removed.

We first examined all the counts for all the readouts (binned in a strong emission feature, a continuum region, and the whole 500 diode region) as a function of time and looked for short-term variations. Variations in the dark count as a function of the position of *HST* in its orbit were readily apparent. No short-term variations such as those reported by Soderblom et al. (1996), believed due to telescope “breathing” and calibration lamp voltage fluctuations, were evident. We did not expect any, because we used the LSA for our observations. There was an increase in observed flux at several wavelengths around phase 1906.6, but no other obvious flares (i.e., count rates $\geq 3 \sigma$ above the mean level) were detected. Low-level “micro-flaring” cannot be ruled out. Because of the low count rate even during the well-defined flare, short flares could not be distinguished from random noise. We could not use a high count rate in successive readouts as an indication of a flare, because even during the strong flare around phase 1906.6 most elevated readouts were not adjacent to each other. To determine the cutoff value, we looked at all the counts in a region thought to be relatively free of known emission lines and believed to represent continuum. In this way, we could determine the minimum, maximum, and mean count rate per diode per readout expected. From this we concluded that a cutoff of 25 counts per readout was a reasonable choice. As a check, we adjusted the cutoff until the sum of the rejected readouts showed a statistically significant number of counts above the mean in the regions of the strong emission lines (i.e., Fe XXI and O V). Again, a cutoff of 25 yielded reasonably clean spectra. Although this method poses some danger of removing real fluctuations, the rejected readouts are randomly scattered throughout each observation and amount to approximately 2% of the total exposure. The major rise in count rate during observation Z364060CT started around readout 554 and continued until about scan 1161. This is only approximate, because many readouts in between show zero counts. Co-adding all these spectra was still not sufficient to obtain a flare spectrum with a useful signal-to-noise ratio.

In Figure 5 we show the flux as a function of time during the Z364060CT exposure binned in 5 s intervals in three wavelength bands. The top light curve shows the flux in the entire 500 diode range as a function of time. A sharp rise followed by a gradual decay is seen, possibly with a second, smaller flare around 1850 s after the start of the exposure. In an attempt to determine whether the flare occurred in the Fe XXI coronal feature, we also computed the total flux in a region centered on the Fe XXI and O I feature (*middle*), the latter being included because it is heavily blended with the Fe XXI emission. Finally, we did the same for a region as free of lines as possible (*bottom*). As we show below this is not really a line-free region, but we obtained the same results for any other region we sampled. The flux increased over the entire wavelength range, not just in a few strong lines. To clearly see the time history, these data have not been cleaned in any way, so some of the smaller spikes are due most likely to noisy readouts.

Because of the resolution of the data in RAPID mode, the previously split RAPID exposures were co-added, representing an integration time of nearly 75 minutes (Table 2).

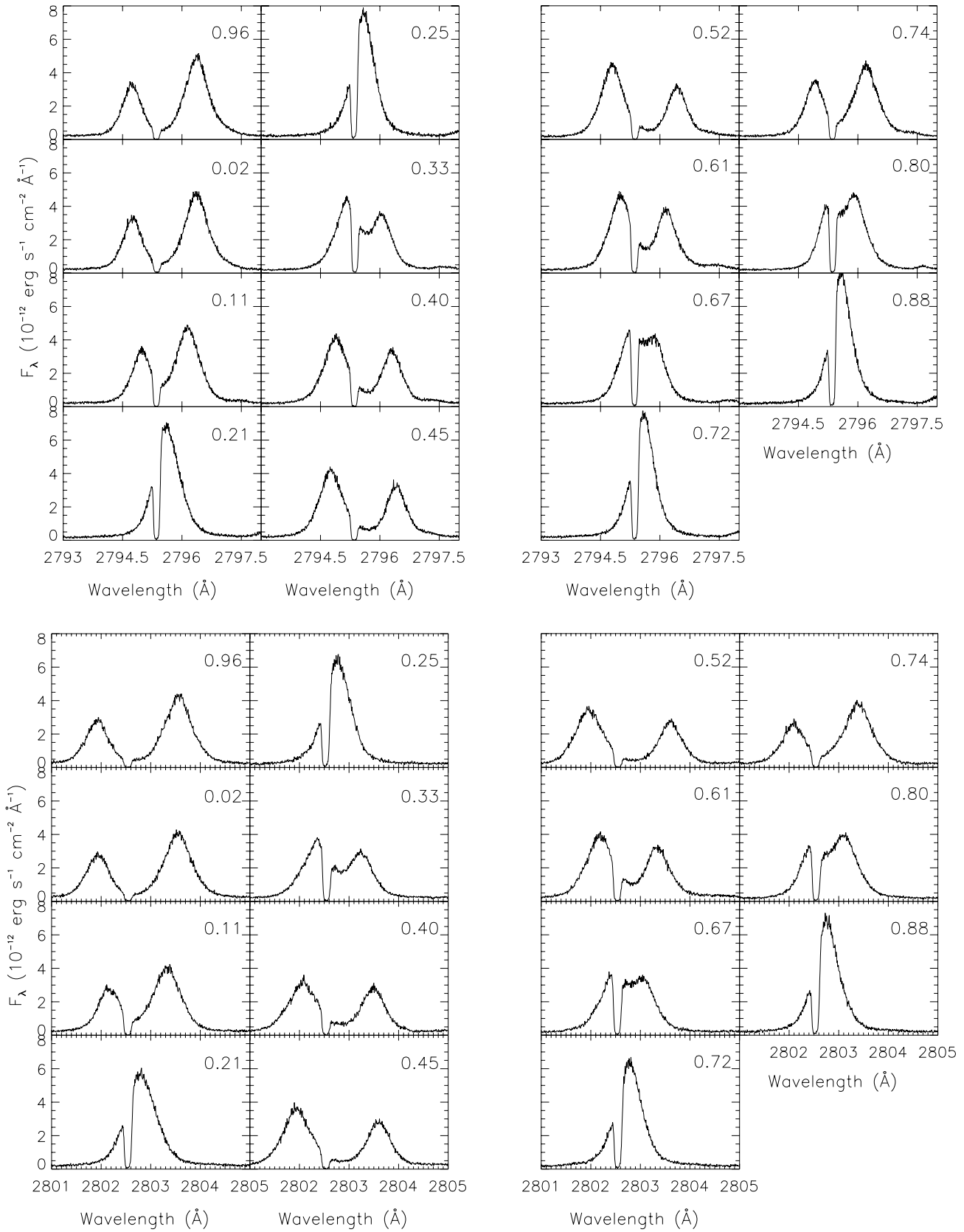


FIG. 1.—All *HST* GHRS Mg II *k* (2795.530 Å) and *h* (2802.695 Å) spectra as a function of time, showing orbital phase (*upper right*; see Table 1) for each. Emission lines from each star shift are due to the binary motion. The absorption is interstellar.

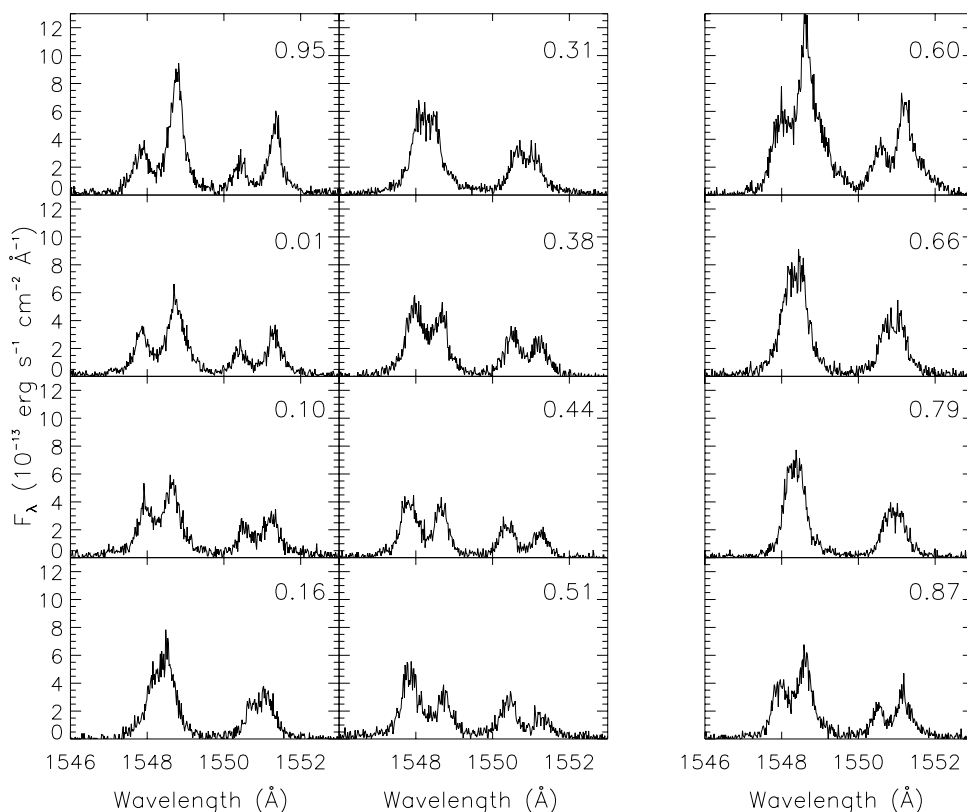


FIG. 2.—All *HST* GHRS C IV (1548.202 + 1550.774 Å) spectra as a function of time, showing orbital phase (*upper right*; see Table 1) for each. Emission lines from each star shift are due to the binary motion.

Because the extracted flare spectrum has a low signal-to-noise ratio and because the flare occurred over the entire wavelength region, we increased the cutoff to 40 during the 554–1161 readouts in Z364060CT. As a result, some additional noise is included.

Final calibration was performed in the same manner as for the ACCUM spectra, but an extra calculation was required to correct for the dark count rate. The dark counts, as a function of geomagnetic latitude and longitude, were calculated from the Lindler (1995) models and subtracted from the cleaned spectrum. Because of small count statistics, the integrated dark count rate was subtracted from

the co-added spectrum rather than from individual readouts before being summed. All spectra of the Fe XXI region as a function of time are shown in Figure 6. In some cases, the mean “continuum” level in the calibrated RAPID spectra is slightly below zero, probably because the empirically derived Lindler (1995) model overestimates the detector dark current.

2.2. EUVE Observations

The extreme ultraviolet (EUV) spectral region includes emission lines arising from the upper transition region and lower corona, bridging the gap between ultraviolet and

TABLE 2
RAPID READOUT PROCESSING LOG

Phase ^a	Observation	n^b	n_r^c	c^d	Observation	n^b	n_r^c	c^d
1905.98	Z364010GT	2258	32	25.88	Z364010IT	2231	41	24.64
1906.04	Z364010ST	2249	52	28.83	Z364010UT	2262	50	27.73
1906.14	Z364020ET	2263	50	26.35	Z364020GT	2248	53	29.97
1906.19	Z364020MT	2262	95	28.23	Z364020OT	2255	44	24.36
1906.28	Z364030AT	2053	36	20.80	Z364030CT	2052	46	21.62
1906.49	Z364040ET	2264	68	22.38	Z364040GT	2263	33	23.61
1906.55	Z364040QT	2200	42	26.08	Z364040ST	2247	37	25.68
1906.64	Z364050ET	2255	50	25.89	Z364050GT	2204	47	25.74
1906.70	Z364050QT	2247	59	25.55	Z364050ST	2246	58	26.15
1906.76	Z364060AT	2052	89	24.75	Z364060CT	2033	89 ^e	18.02
1906.82	Z364060MT	2047	37	20.59	Z364060OT	2034	116	21.40

^a Mean orbital phase of combined observations.

^b Number of readouts.

^c Number of rejected readouts.

^d Integrated dark counts.

^e During the readouts between 554 and 1161 the cutoff was raised to 40.

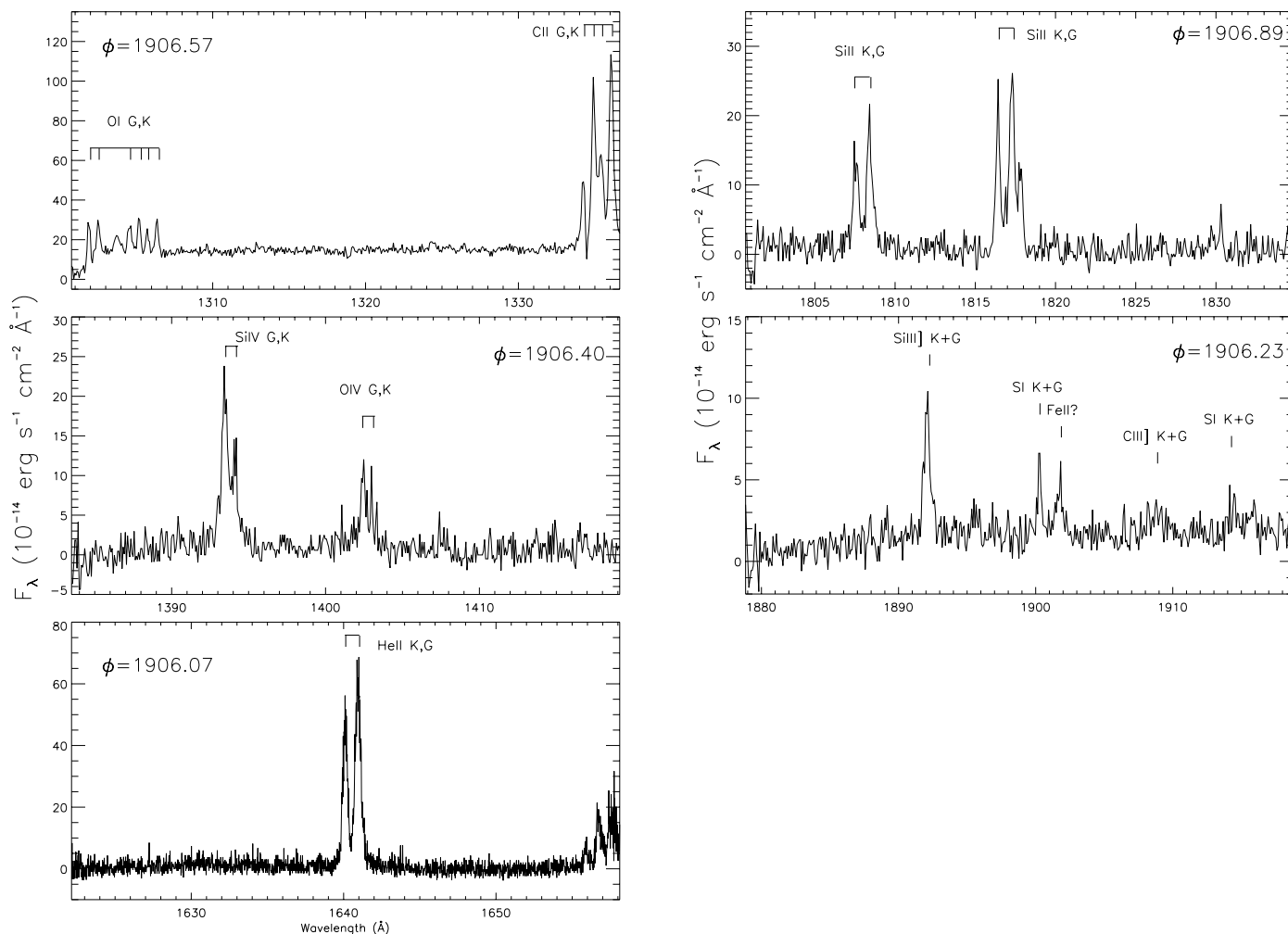


FIG. 3.—Miscellaneous GHRSS spectra obtained at other wavelengths, with key features indicated. Except for the He II region, these spectra have been smoothed over 4 bins.

X-ray observations. V824 Ara was observed with the *Extreme Ultraviolet Explorer (EUVE)* spacecraft for 44 ks. We used the short (SW), medium (MW), and long (LW) wavelength and the deep survey (DS) detectors. The DS

photometer uses a Lexan-Boron filter with an effective bandpass of 40–190 Å, peaking around 90 Å. The entire DS light curve is shown in Figure 7. The first half of the EUV light curve was simultaneous with the *HST* observations. One or two flares occurred during the first cycle (V824 Ara orbit 1906), and the light curve exhibited considerable variability during the second cycle.

V824 Ara was not in the *EUVE* continuous viewing zone, so the observations contain gaps when the target was occulted by the Earth. Because a target of opportunity interrupted the observing program, this exposure time is less than half of that planned, and the resulting spectrum is weak. Because of the low count rate, insufficient counts were available to bin the spectra by time, even with a coarse sampling. All spectra were reduced using the *EUVE*-specific IRAF software and were processed using the optimal extraction routines to maximize signal-to-noise ratio. In Figure 8 we show the SW spectrum only, because no emission features could be detected in the MW and LW bands. At this resolution (each channel equals 0.2 Å, or 900 km s⁻¹), and with a full cycle of orbital motion during the integration causing considerable phase smearing, the two stellar components are not separable. In this spectrum the Fe XVIII (93.93 Å), Fe XXIII + Fe XX (132.8 Å), and Fe XIX 108.37 Å are clearly visible, while some weaker lines are

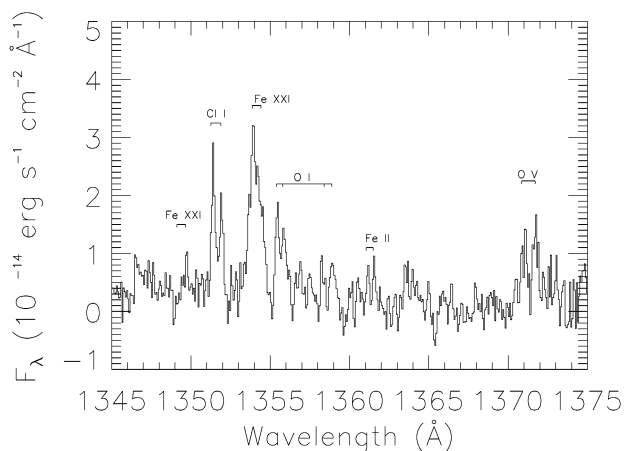


FIG. 4.—Lone *HST* GHRSS ACCUM spectrum of the Fe XXI region (Z364030LT; all others were obtained in RAPID mode), with several key features identified.

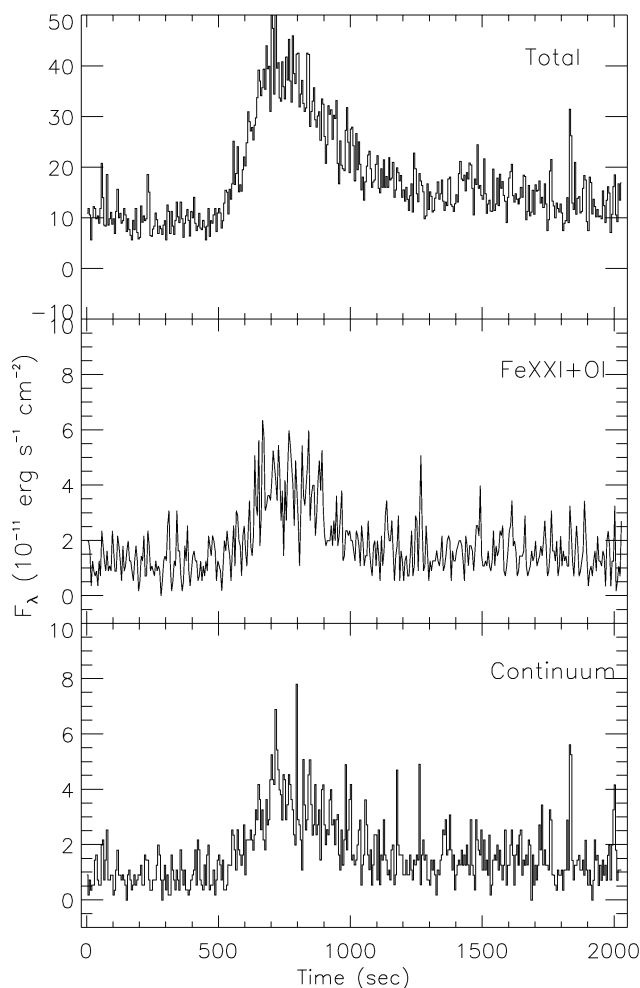


FIG. 5.—Time history of flare as observed in the Fe XXI region GHRIS spectra, showing the integrated flux over the entire 500 diode range as a function of time, with zero corresponding to the start of the Z364060CT exposure (*top*), and the integrated flux in two 46 diode wavelength regions, the first centered on the Fe XXI + O I features (*middle*) and the second covering a line-free region ($\approx 1345\text{--}1347\text{ \AA}$; *bottom*). A bin size of 5 s is used for all panels, and the dark count rate has been removed. These data have not been “cleaned” of noisy readouts and include the entire observation.

marginally detected. Counts due to the flare are included in this spectrum.

2.3. Radio Observations

Radio observations are unique in their ability to detect the presence and production of nonthermal electron populations within strong magnetic fields in stellar coronae. On the Sun, the first—and primary—observational signature of a flare is usually the detection of impulsive radio emission at centimeter wavelengths produced by gyrosynchrotron emission from nonthermal electrons. These electrons subsequently precipitate into the chromosphere, producing hard X-ray and ultraviolet chromospheric emission, and they evaporate hot gas into the corona to produce extreme ultraviolet and soft X-ray emission. Thus, although physically unrelated, the nonthermal radio-emitting electron population plays an important role in energizing the particle population emitting at other wavelengths. The radio emission of the Sun is dominated by nonthermal processes only

during flares. The radio emission of active late-type stars, however, seems to be dominated by nonthermal processes even during periods of weak and relatively steady emission, which may define a quiescent level of emission for the star.

To detect the presence and production of nonthermal electrons in its corona, we observed V824 Ara for four consecutive days from 1996 April 30 to May 3 with the Australia Telescope Compact Array (ATCA). V824 Ara is visible for nearly 18 hr each day from the ATCA, and we were generously allocated 16.5 hr observing time for this star on each of the four days (although short amounts of observing time were lost on each of the last three days because of technical problems).

The ATCA is able to observe at two wavelengths simultaneously in either the 20 and 13 cm bands or the 6 and 3 cm bands, or it can time share between all four bands. Because the broadband radio continuum emission, the component usually attributed to nonthermal gyrosynchrotron emission, of G and early K dwarfs usually has a flat to rising spectrum between 20 and 3 cm (e.g., Lim et al. 1994), we observed (simultaneously) at 6 and 3 cm only. Our observing sequence usually comprised ~ 15 minute scans of V824 Ara interleaved by ~ 1.5 minute scans of a secondary calibrator, the unresolved extragalactic object PKS 1718–649. For absolute flux calibration, we used the primary flux calibrator PKS 1934–638.

After calibrating the measured visibilities in all four Stokes parameters, we imaged the data obtained on each day and at each wavelength separately. There are few confusing sources in the field, which is dominated by the emission of V824 Ara. We subtracted the confusing sources from the measured visibilities and then performed a Fourier transform of the remaining visibilities at the radio position of V824 Ara to obtain the radio light curve of the binary system. The results are shown in Figure 9, where we have plotted both the total intensity (Stokes I) and the circularly polarized intensity (Stokes V) of V824 Ara at each wavelength on each of the four days as a function of time. Only the first day’s data were obtained simultaneously with the *HST* observations.

2.4. Visual Spectroscopic Observations

Visual spectra include a large number of diagnostics of stellar photospheres. We optimized our observations to obtain high signal-to-noise ratio and high time resolution of lines in the 6300 to 6600 Å region that are used to derive Doppler images of the stellar surface.

2.4.1. Cerro Tololo Inter-American Observatory

From 1996 April 30 to May 5, we used the 1.5 m telescope at Cerro Tololo Inter-American Observatory (CTIO) to obtain over 100 spectra of V824 Ara during the period covered by this campaign. The first two night’s data were obtained simultaneously with the *HST* observations. We used the number 3 Tektronix CCD (2048×2048 24 μm pixels) at the bench-mounted echelle spectrograph. With appropriate gratings and filters, we obtained complete wavelength coverage from 5140 to 7775 Å in 37 orders. Typical signal-to-noise ratios in these 15–20 minute exposures were greater than 200:1 in the continuum near the lines of interest. The 2 pixel resolution was about 65,000. We also observed appropriate telluric, spectroscopic, and radial velocity standards. Primary wavelength calibration

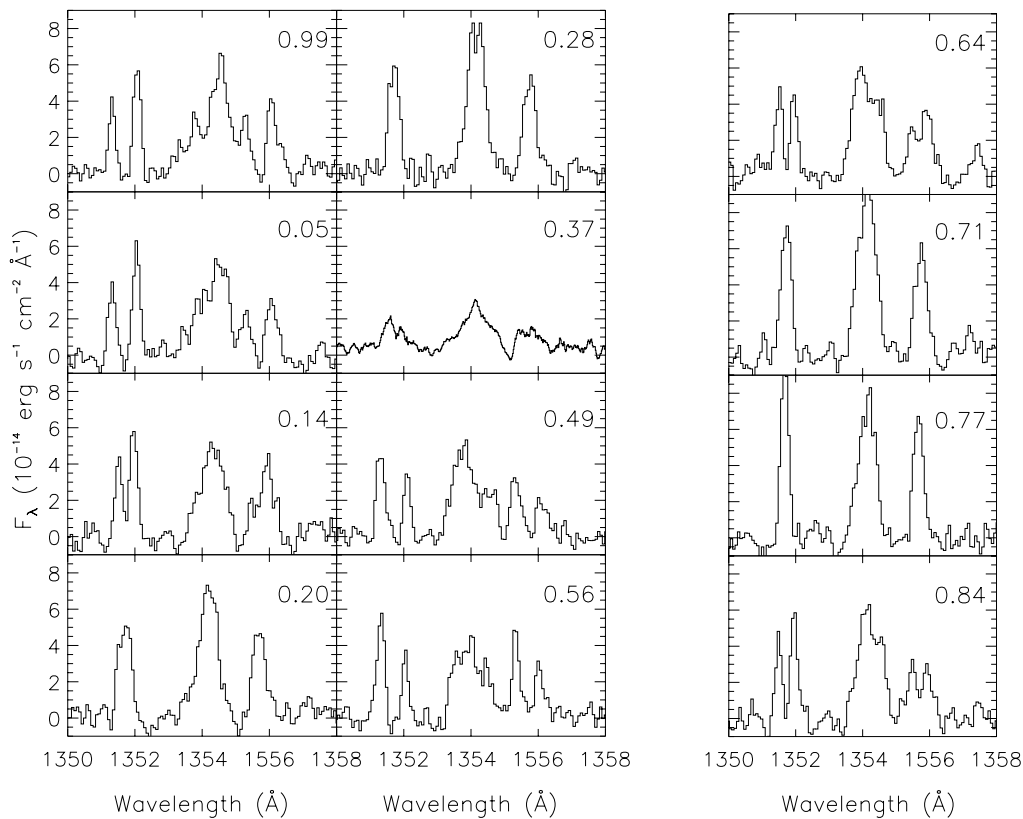


FIG. 6.—Final reduced spectra of the Fe XXI (1354.14 Å) region as a function of time. See Fig. 4 for line identifications. The spectrum shown at phase 0.37 was obtained in ACCUM mode; all others were obtained in RAPID mode.

was performed using spectra of a ThAr lamp obtained every several hours.

2.4.2. European Southern Observatory

High-resolution visual spectroscopy for Doppler imaging was also carried out at ESO during seven nights from 1996 May 18 to 23, three weeks after the *HST* observations. The 1.4 m coude auxiliary telescope was used with the coude echelle spectrograph in single-order mode. Together with the Loral 2688×512 $15 \mu\text{m}$ pixel CCD, the spectrograph provided a resolving power of 70,000 (3 km s^{-1}) in a useful

wavelength range of around 70 \AA . All integrations were set at an exposure time of 20 minutes, have typical signal-to-noise ratios of 250:1, and were centered at 6425 \AA . This sequence allowed for a reasonably good phase sampling with a total of 29 spectra but contained two 0.17 phase gaps near 0.2 and 0.7 due to bad weather.

The Doppler images resulting from these data are presented by Strassmeier & Rice (2000). Although spots can evolve on a rotational timescale, it is likely that the gross features observed in their Doppler maps can be applied to the observations reported here, since the light curve appears

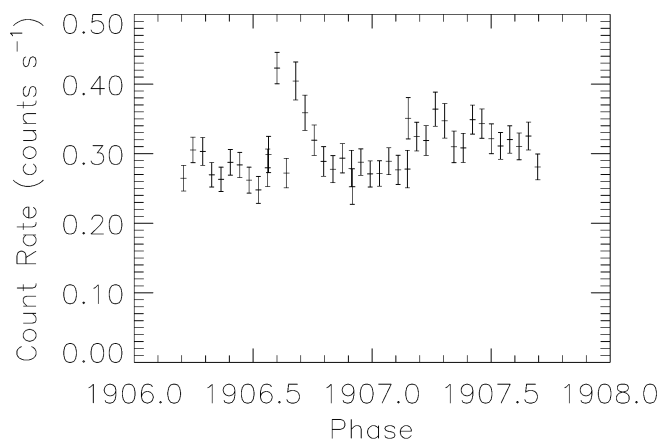


FIG. 7.—Entire EUVE DS light curve as a function of orbital time. Each point represents an average over one spacecraft orbit (approximately 95 minutes).

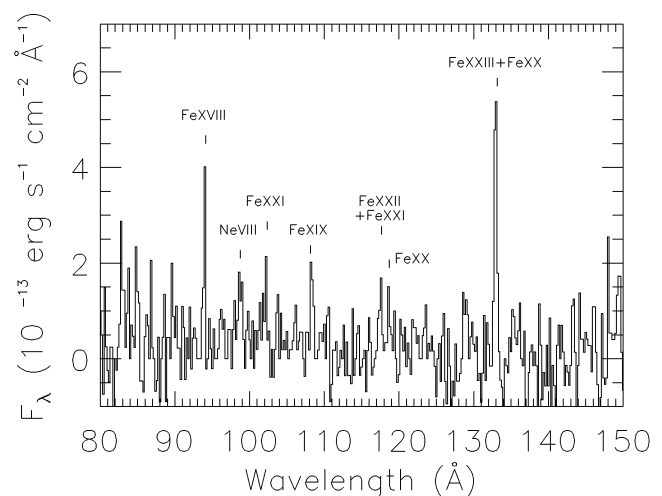


FIG. 8.—EUVE SW spectrum with several key lines indicated

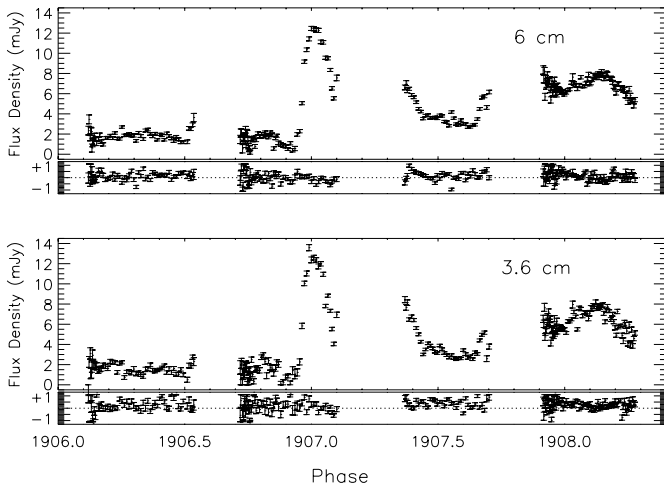


FIG. 9.—Radio flux density (Stokes *I*) and circular polarization (Stokes *V*) obtained at the Australia Telescope.

not to have changed in the interim. Furthermore, Strassmeier & Rice (2000) confirmed some of the same surface features observed by Hatzes & Kürster (1999), suggesting that at least some of the features are long lived.

2.5. Visual Photometric Observations

Four sites around the world—professional and amateur observatories—provided us with simultaneous and contemporaneous broadband photometry (Table 3). All data were taken differentially with respect to the comparison stars HD 156427 (K4–K5 III) and HD 154775 (K5–M0 III). After excluding bad nights and grossly deviant points, we retained the South African Astronomical Observatory (SAAO) data plus two nights from Mount John University Observatory (MJUO) and one night each from Auckland and Waiharara. However, wavelength dependent zero-point shifts with respect to the SAAO data were evident from the check-star and comparison-star magnitudes. These have been corrected for by simply determining average difference between the check and comparison magnitudes and shifting them to the respective SAAO values. The MJUO – SAAO shifts were -0.01 in *V*, $+0.025$ in *B*–*V*, -0.01 in *V*–*R*, and inconsistent in *U*–*B*. The Auckland – SAAO and Waiharara – SAAO shifts were -0.02 in *V* and also inconsistent in the *U* and *B* band-passes. The complete data set will be used in conjunction with the visual spectra to construct photospheric images.

3. RESULTS

3.1. Variability

One of our primary goals is to compare variability of diagnostics of all atmospheric levels, from the photosphere to the corona. We can measure the line flux and line profile shape as a function of phase for the ultraviolet lines. Fea-

tures of similar strength are observed from each of the stellar components of V824 Ara in high-resolution spectra. This makes measuring the line properties of the individual stars near orbital conjunction virtually impossible. For example, the 1345–1360 Å region spectra show the lines blended in almost half the observed phases (Fig. 6.) Fitting the line profiles at phases near conjunction requires fixing many or all of the parameters to the values observed near orbital quadrature. The situation is better for the echelle spectra, but line blends, e.g., the subordinate 2797.998 Å line of the Mg II *k* profile, are still prevalent.

To measure line fluxes we fitted the profiles with single Gaussians when possible. The adjacent continuum was fitted with a quadratic. In Tables 4 and 5 we list the fluxes of the lines measured in this fashion. Several lines, He II, Si IV, C IV, and Mg II could not be fitted with a single-emission component for each star. In Table 6 we list fluxes derived from two-component (broad + narrow) fits to these lines. The values for C IV and Mg II are given for a representative quadrature phase. Line profile fits are discussed in more detail in § 3.3. For our total flux variability study, we report in Tables 7 and 8 the integrated line flux above the continuum from both stars.

The lines in the integrated EUVE spectrum (Fig. 8) were also fitted with single Gaussian components. The two stellar components are not resolved in these spectra. Line identifications and integrated line flux measurements are listed in Table 9.

In Figure 10 we compare the flux variation for key indicators of all atmospheric levels over the cycle covered by the *HST* observations. The visual photometry shows a rotational modulation of about 0.075 mag peak to peak, with a minimum around $\Phi = 0.75$. This is presumably due to starspots on either or both components. None of the other indicators show any clear evidence for rotational modulation. In fact, the radio (Fig. 9) and EUV (Fig. 7) show variation from one cycle to the next. Most of the variation can be interpreted as a series of flares.

3.2. Flares

To determine the flare enhancement or timescales, it is first necessary to determine the baseline level of emission. However, at the start of the observations both Mg II and C IV appear to be on a decline. While this could represent a decay phase of a flare, it also corresponds to a brightening in the *V* band. Therefore, it is not possible to distinguish this behavior from rotational modulation. Unfortunately, there are no radio data during these observations. During these observations the Mg II and C IV components centered near the radial velocity of the G star show an enhancement over spectra obtained from phases 1906.2 to 1906.4. This modulation or flare may correspond to the lower latitude spot found in the Strassmeier & Rice (2000) images at this phase.

TABLE 3
OBSERVING LOG: OPTICAL PHOTOMETRY

Observatory	Observer	System	JD – 2,445,000	Nights	Data Points
SAAO, South Africa	D. Kilkenny et al.	<i>UBV(RI)_C</i>	197–214	7	62
MJUO, NZ	E. Budding	<i>UBV(RI)_C</i>	203–206	3	60
Waiharara, NZ	W. S. G. Walker	<i>UBV</i>	200–210	6	140
Auckland, NZ	H. O. Williams	<i>UBV</i>	205–207	2	40

TABLE 4
GAUSSIAN FIT RESULTS: Fe XXI REGION (1345–1360 Å)

Line and Phase	G FLUX (10^{-14} ergs s $^{-1}$ cm $^{-2}$)	K FLUX (10^{-14} ergs s $^{-1}$ cm $^{-2}$)	G FWHM (km s $^{-1}$)	K FWHM (km s $^{-1}$)	G ΔV^a (km s $^{-1}$)	K ΔV^a (km s $^{-1}$)
Cl I 1351.657 Å:						
1905.98	1.67 ± 0.01	1.00 ± 0.01	55 ± 1	50 ± 1	3 ± 1	14 ± 1
1906.04	1.67 ± 0.04	1.09 ± 0.04	55 ± 1	56 ± 2	3 ± 1	9 ± 1
1906.14	1.89 ± 0.01	1.26 ± 0.01	61 ± 1	54 ± 1	13 ± 1	22 ± 1
1906.19		2.66 ± 0.01		99 ± 1
1906.28		2.52 ± 0.01		83 ± 1
1906.35	0.87 ± 0.03	0.62 ± 0.03	73 ± 10	67 ± 16	0 ± 4	-6 ± 6
1906.49	1.47 ± 0.01	0.86 ± 0.01	64 ± 1	47 ± 1	6 ± 1	4 ± 1
1906.55	1.81 ± 0.25	0.93 ± 0.25	62 ± 3	49 ± 5	1 ± 1	-2 ± 2
1906.64	1.37 ± 0.01	1.20 ± 0.01	58 ± 1	51 ± 1	15 ± 1	7 ± 1
1906.70		3.08 ± 0.01		83 ± 1
1906.76		3.12 ± 0.14		62 ± 1
1906.82	1.66 ± 0.01	1.15 ± 0.01	55 ± 1	38 ± 1	-1 ± 1	52 ± 1
Fe XXI 1354.14 Å:						
1905.98	3.33 ± 0.01	2.51 ± 0.01	119 ± 1	211 ± 4	8 ± 1	14 ± 2
1906.04	1.71 ± 0.31	3.63 ± 0.36	99 ± 5	229 ± 12	23 ± 2	78 ± 8
1906.14	2.48 ± 0.63	2.30 ± 0.49	134 ± 4	154 ± 6	23 ± 4	35 ± 7
1906.19		5.31 ± 0.01		149 ± 1
1906.28		5.63 ± 0.01		139 ± 1
1906.35	1.86 ± 0.03	1.03 ± 0.03	150 ± 10	145 ± 36	-3 ± 9	2 ± 17
1906.49	3.97 ± 0.01	1.02 ± 0.01	164 ± 1	84 ± 1	2 ± 1	4 ± 1
1906.55	2.89 ± 3.10	2.60 ± 3.68	157 ± 19	194 ± 40	-17 ± 15	-39 ± 28
1906.64	3.72 ± 0.01	1.75 ± 0.01	125 ± 1	91 ± 2	4 ± 1	20 ± 1
1906.70		6.82 ± 0.01		146 ± 1
1906.76		5.37 ± 0.14		138 ± 3
1906.82	1.06 ± 0.03	4.13 ± 0.04	63 ± 2	134 ± 2	-39 ± 1	56 ± 1
O I 1355.598 Å:						
1905.98	1.53 ± 0.01	1.13 ± 0.01	78 ± 1	76 ± 1	21 ± 1	18 ± 1
1906.04	1.22 ± 0.04	0.81 ± 0.04	78 ± 3	68 ± 3	22 ± 1	19 ± 1
1906.14	2.29 ± 0.01	0.40 ± 0.01	111 ± 1	37 ± 1	21 ± 1	19 ± 1
1906.19		2.49 ± 0.01		102 ± 1
1906.28		2.56 ± 0.01		98 ± 1
1906.35	0.43 ± 0.05	0.76 ± 0.07	52 ± 16	124 ± 46	15 ± 6	-6 ± 18
1906.49	1.28 ± 0.01	0.88 ± 0.01	79 ± 1	92 ± 1	22 ± 1	20 ± 1
1906.55	1.41 ± 0.28	1.29 ± 0.26	58 ± 4	97 ± 9	20 ± 2	8 ± 4
1906.64	0.83 ± 0.01	1.66 ± 0.01	64 ± 2	91 ± 2	19 ± 1	12 ± 1
1906.70		2.95 ± 0.01		98 ± 1
1906.76		2.89 ± 0.14		82 ± 2
1906.82	1.10 ± 0.02	1.28 ± 0.02	77 ± 3	90 ± 3	-34 ± 1	70 ± 1
O V 1371.292 Å:						
1905.98	1.17 ± 0.01	0.50 ± 0.01	101 ± 1	71 ± 1	22 ± 1	28 ± 1
1906.04	0.47 ± 0.01	0.32 ± 1.46	54 ± 3	77 ± 2	7 ± 1	36 ± 2
1906.14	0.88 ± 0.12	0.80 ± 0.15	67 ± 6	92 ± 12	34 ± 2	24 ± 5
1906.19		1.70 ± 0.01		130 ± 2
1906.28		0.27 ± 0.01		30 ± 2
1906.35	0.65 ± 0.05	0.63 ± 0.05	117 ± 5	92 ± 5	-10 ± 1	32 ± 1
1906.49	0.78 ± 0.01	0.72 ± 0.01	88 ± 1	76 ± 1	29 ± 1	21 ± 1
1906.55	0.96 ± 0.35	0.85 ± 0.41	96 ± 16	112 ± 24	24 ± 6	15 ± 10
1906.64	0.49 ± 0.01	1.00 ± 0.01	56 ± 2	89 ± 1	34 ± 1	19 ± 1
1906.70		0.53 ± 0.01		67 ± 1
1906.76		1.73 ± 0.19		109 ± 8
1906.82	0.89 ± 0.01	1.12 ± 0.01	78 ± 1	127 ± 2	-27 ± 1	71 ± 3

^a Radial velocity with respect to predicted orbital velocity.

A well-observed flare can be clearly seen in the *EUVE*, C IV, and Mg II light curves around phase 1906.60. It appears from the *EUVE* DS count rate that either two flares were observed or one with a complex behavior. The first peak was clearly detected in C IV, was possibly observed in the Mg II lines, but was missed because of an observing gap in the 1345–1360 Å region. It is probable that

the rise in the radio flux at the end of the first day's observing was a precursor or the beginning of this flare. The second *EUVE* DS peak corresponds to the flare observed in the 1345–1360 Å bandpass (see Fig. 5). Note that although the rise in flux in the Fe XXI + O I bandpass appears to be a marginal detection, the flare spectrum is combined with the nonflaring portion of Z364060CT and all of Z364060AT.

TABLE 5
ONE-COMPONENT GAUSSIAN FIT RESULTS

LINE (Å)	PHASE	FLUX (10^{-14} ergs s^{-1} cm^{-2})		FWHM (km s^{-1})		ΔV (km s^{-1}) ^a	
		G	K	G	K	G	K
O I 1304.858	1906.57	5.12 ± 0.01	4.63 ± 0.01	77 ± 1	53 ± 1	8 ± 1	-9 ± 1
O I 1306.029	1906.57	3.05 ± 0.01	4.42 ± 0.01	56 ± 1	56 ± 1	2 ± 1	-11 ± 1
Si IV 1393.755	1906.40	10.39 ± 0.34	4.89 ± 0.32	110 ± 6	90 ± 8	1 ± 2	1 ± 3
Si IV 1402.770	1906.40	3.99 ± 0.52	2.63 ± 0.88	83 ± 11	112 ± 37	-3 ± 5	-20 ± 16
He II 1640.428	1906.07	28.72 ± 0.08	19.37 ± 0.08	83 ± 1	71 ± 1	15 ± 1	19 ± 1
Si II 1808.012	1906.89	5.71 ± 0.07	7.84 ± 0.07	69 ± 2	73 ± 2	-7 ± 1	-3 ± 1
Si II 1816.928	1906.89	6.63 ± 0.01	9.63 ± 0.03	49 ± 1	58 ± 1	-18 ± 1	-9 ± 1
Si II 1817.451	1906.89	1.73 ± 0.53	4.18 ± 0.02	46 ± 5	53 ± 1	-29 ± 1	-8 ± 1
Si III] 1892.030	1906.23	4.69 ± 0.54		92 ± 13	
S I 1900.268	1906.23	1.44 ± 0.55		45 ± 14	
C III] 1908.734	1906.23	1.63 ± 0.54		204 ± 120	
S I 1914.698	1906.23	1.53 ± 0.52		154 ± 79	

^a Radial velocity with respect to predicted orbital velocity.

No obvious rise in Mg II is detected at the second *EUVE* DS peak, and there is no concurrent C IV observation. Osten & Brown (1999) interpret this as an example of a “sympathetic” flare. The C IV spectrum obtained at $\Phi = 1906.60$ (Fig. 2) shows that the flare emission was centered at the radial velocity of the K star. This phase is near the light minimum in the *V* light curve, and Strassmeier & Rice (2000) find that this phase corresponds to the maximum visibility of the lower latitude spots on the G star. On the K star at this phase their Doppler maps show no large equatorial spot, but the polar feature is directly in view.

Just after the end of the *HST* coverage, a large radio flare began. It had a symmetric light curve. No circular polariza-

tion was detected, with an upper limit as low as 6% (3σ). The EUV emission remained constant throughout this flare. The third day’s radio observation begins with what appears to be the decay phase of a flare that occurred between phase 1907.1 and 1907.3. This corresponds to the time when the EUV light curve became enhanced and highly variable. Near the beginning of this flare, the degree of circular polarization was nearly 100%, which suggests a coherent emission mechanism such as an electron-cyclotron maser.

Higher radio emission and possible flaring activity may also be present around phases 1907.7 and 1908.1. At this phase, the visible hemisphere is the same as during the strongest radio flare, at 1907.0. This suggests that the hemi-

TABLE 6
TWO-COMPONENT GAUSSIAN FIT RESULTS

LINE AND PHASE	FLUX (10^{-14} ergs s^{-1} cm^{-2})		FWHM (km s^{-1})		ΔV (km s^{-1}) ^a	
	G	K	G	K	G	K
He II 1640.428 Å:						
1906.07 ^b	24.68 ± 0.20	17.21 ± 0.15	76 ± 1	67 ± 1	15 ± 1	19 ± 1
1906.07 ^c	9.18 ± 0.59	...	359 ± 24	...	7 ± 12	...
Si IV 1393.755 Å:						
1906.40 ^b	4.41 ± 0.81	1.68 ± 0.43	67 ± 9	48 ± 11	1 ± 2	3 ± 3
1906.40 ^c	7.14 ± 0.50	3.70 ± 0.40	224 ± 36	226 ± 57	1 ± 2	4 ± 3
C IV 1548.202 Å:						
1905.95 ^b	8.77 ± 0.18	8.69 ± 0.08	62.2 ± 5.0	65.6 ± 4.3	18.1 ± 1.0	15.2 ± 1.0
1905.95 ^c	20.09 ± 0.48	10.78 ± 0.17	170.1 ± 12.2	223.3 ± 23.2	18.1 ± 1.0	15.2 ± 1.0
C IV 1550.774 Å:						
1905.95 ^b	7.00 ± 0.12	4.43 ± 0.08	73.4 ± 7.3	57.7 ± 7.0	21.1 ± 1.5	18.6 ± 1.7
1905.95 ^c	9.71 ± 0.30	5.20 ± 0.22	204.8 ± 43.8	209.6 ± 26.0	21.1 ± 1.5	18.6 ± 1.7
Mg II <i>k</i> 2795.530 Å:						
1905.96 ^b	78.4 ± 2.2	58.8 ± 5.5	46.1 ± 3.7	43.3 ± 6.1	5.1 ± 0.8	0.7 ± 1.1
1905.96 ^c	282.2 ± 4.9	135.7 ± 10.7	94.7 ± 3.3	81.2 ± 6.4	4.1 ± 0.7	1.8 ± 1.3
1905.96 ^d	7.0 ± 0.1	7.9 ± 0.1	41.8 ± 13.1	52.6 ± 15.0	4.6 ± 5.6	≡ 0
Mg II <i>h</i> 2802.695 Å:						
1905.96 ^b	0.32 ± 0.01	0.80 ± 0.03	55.7 ± 9.1	78.0 ± 7.6	-8.1 ± 1.0	-2.8 ± 2.0
1905.96 ^c	2.50 ± 0.03	0.80 ± 0.07	140.7 ± 4.6	170.0 ± 24.4	-6.2 ± 0.7	-4.8 ± 1.7

^a Radial velocity with respect to predicted orbital velocity.

^b Narrow component.

^c Broad component.

^d Subordinate Mg II *k* line at 2797.998 Å.

TABLE 7
INTEGRATED Mg II LINE
FLUXES^a

Phase	h	k^b
1905.96.....	4.36	5.58
1906.02.....	4.29	5.46
1906.11.....	4.04	5.32
1906.21.....	3.63	4.77
1906.25.....	3.63	4.76
1906.33.....	3.53	4.78
1906.40.....	3.56	5.06
1906.45.....	3.87	5.12
1906.52.....	3.63	5.10
1906.61.....	4.13	5.54
1906.67.....	3.46	4.78
1906.72.....	3.58	4.73
1906.74.....	3.70	4.79
1906.80.....	3.66	4.88
1906.88.....	3.90	5.31

^a Units are 10^{-12} ergs s^{-1} cm^{-2} .

^b Includes subordinate line.

spheres facing the observer at this quadrature phase are very active. As the ultraviolet flare occurred on almost the opposite hemisphere, there does not appear to be one particular active longitude.

Throughout our radio observations, the radio spectrum of V824 Ara between 6 and 3 cm was gently falling (spectral

TABLE 8
INTEGRATED C IV LINE FLUXES

Phase	Flux (10^{-13} ergs s^{-1} cm^{-2})
1905.95.....	9.49
1906.01.....	7.54
1906.10.....	7.33
1906.16.....	7.82
1906.31.....	8.54
1906.38.....	8.83
1906.44.....	6.65
1906.51.....	7.01
1906.60.....	16.79
1906.66.....	10.34
1906.79.....	7.57
1906.87.....	7.85

TABLE 9
EUVE LINE FLUXES

ID ^a	Flux (10^{-14} ergs s^{-1} cm^{-2})
Fe xxviii.....	9.98
Ne viii.....	12.32
Fe xxi.....	11.17
Fe xix.....	9.74
Fe xxii + Fe xxi.....	9.28
Fe xx.....	7.28
Fe xxiii + Fe xx.....	29.44

^a See Fig. 8.

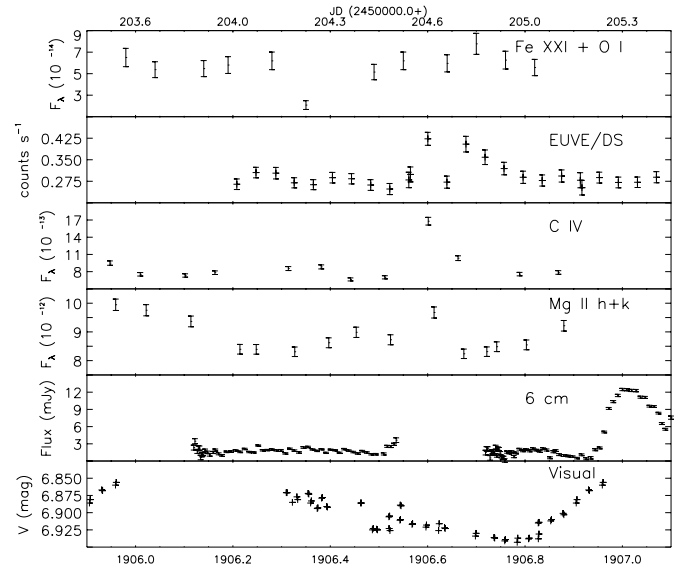


FIG. 10.—Multiwavelength light curves for V824 Ara as a function of time during the cycle of V824 Ara that was observed with *HST*. Note that the visual photometry is not simultaneous with the other observations but rather a phased set of data as described in the text. Error bars for the GHRS data are estimated from repeated measurements of several lines in each bandpass, purposely choosing overly high and low continuum levels. In this fashion, we conservatively estimate errors of 10%, 5%, and 2% for the Fe XXI + O I, Mg II ($h + k$), and C IV line fluxes, respectively. Placement of the continuum is the largest source of error in these measurements. Note that the fluxes, F_{λ} , are in units of ergs s^{-1} cm^{-2} .

index $\alpha \approx -0.3$) during periods of quiescence and approximately flat ($\alpha \approx 0.0$) during periods of strong flaring. The broadband radio properties of V824 Ara are similar to those usually displayed by other active late-type dwarf stars and are consistent with nonthermal gyrosynchrotron emission. The flat spectrum and low degree of circular polarization suggests that the broadband radio-emitting sources are optically thick. This, together with the detection of a coherent flare during the period of strong flaring, suggests that the broadband radio-emitting sources are significantly smaller than the stellar disk so as not to hide the coherent flare (see White, Kundu, & Jackson 1989). We have searched for any periodic variations in the stellar radio emission. No definitive rotational modulation is seen in the flaring component, as has been seen in the flaring component of AB Dor (Lim et al. 1992, 1994). The presence of strong flares throughout much of our radio observations would have masked any rotationally modulated component in the quiescent stellar emission, as has apparently been seen on EK Dra (Güdel et al. 1995).

3.3. Line Profiles

3.3.1. Gaussian Models

In many situations, the ultraviolet line profiles can be fitted with a Gaussian to measure line flux, profile width, and Doppler shift. With the advent of the GHRS, it has become clear that upper chromospheric and transition region emission lines, such as Mg II, C IV, and Si IV, frequently show non-Gaussian structure in the form of very extended emission wings. Linsky & Wood (1994) discovered that the Si IV and C IV profiles of AU Mic (dMe) include emission wings extending out ± 200 km s^{-1} from line

center. Extended wings were also detected in the RS CVn V711 Tau (=HR 1099; Wood et al. 1996; Dempsey et al. 1996) for Mg II and C IV. Similar wings were detected for Capella (Linsky et al. 1995) but not for the Mg II *h* and *k* lines. The lines of C IV in AB Dor, a young rapidly rotating K0–K2 IV–V single star, also have extended wings (Vilhu et al. 1998). Wood & Linsky (1998) present detailed analysis of C IV and Si IV line wings on several stars.

Since a single Gaussian could not fit the line profiles, two Gaussians were used. Generally, these line fits resulted in a “narrow” component and a “broad” component, which dominates the total line flux. The widths of the narrow feature, 10–50 km s⁻¹, imply that they are broadened primarily by stellar rotation. In contrast, the width of the broad features is typically on the order of 100 km s⁻¹, suggesting a thermal origin. Wood et al. (1996) suggest that the broad Gaussian component arises from “explosive events” similar to microflares, and Wood & Linsky (1998) derive a correlation between the C IV broad component flux and the X-ray surface flux.

As a first step, we modeled all the GHRS profiles with single Gaussians. Our approach is similar to that used by Dempsey et al. (1996). Our fitting used the Marquardt method (Bevington & Robinson 1992) as implemented in IDL programs. Each model includes a polynomial fit to the continuum and one or more Gaussians, each with three free parameters: central wavelength, peak intensity, and Gaussian width. Generally once the continuum was selected it was frozen and not allowed to vary. The Mg II, C IV, and Si IV lines have extended wings for both stellar components. The G star component of the He II 1640 Å profile also appears to possess extended wings. A simple broad + narrow model fits the Si IV profile well, with both components having the same relative velocity with respect to the predicted orbital positions. For He II, the best fit was obtained with a shifted broad component centered closest to the G star radial velocity. The line shift and the shallowness of the Gaussian suggest that some contribution may be coming from extended wings of the K star. However, at the single observed phase and signal-to-noise ratio this cannot be ascertained. Results of these fits are listed in Table 6. In both the single and double Gaussian fits, FWHM values are generally smaller than those observed for other well-studied RS CVn systems such as V711 Tau (Dempsey et al. 1996; Wood et al. 1996), but they are in the range of stars such as β Cet (K0 III) and β Dra (G2 Ib–II; Wood & Linsky 1998).

The C III] profile for V711 Tau appears broad and asymmetric (Dempsey et al. 1996). However, it is not clear from their data whether this is due to an unidentified blend or a transient feature. The C III] line in V824 Ara is considerably broader than if it were a single line. However, because the signal-to-noise ratio is low and the emission from both components is heavily blended ($RV_G = 12.8$ km s⁻¹, $RV_K = -8.0$ km s⁻¹), it is not possible to decompose the profile into multiple components. The Si III] profile at this same phase is slightly asymmetric, as one would expect for the relative line blending, but the width is still not comparable to that of C III].

Representative two-component Gaussian models for C IV and Mg II for a quadrature phase are listed in Table 6 and shown in Figures 11 and 12. The narrow components have smaller FWHM than V711 Tau, although the broad components are comparable in width. Note that in Figure 12 the broad component of the G star totally dominates the

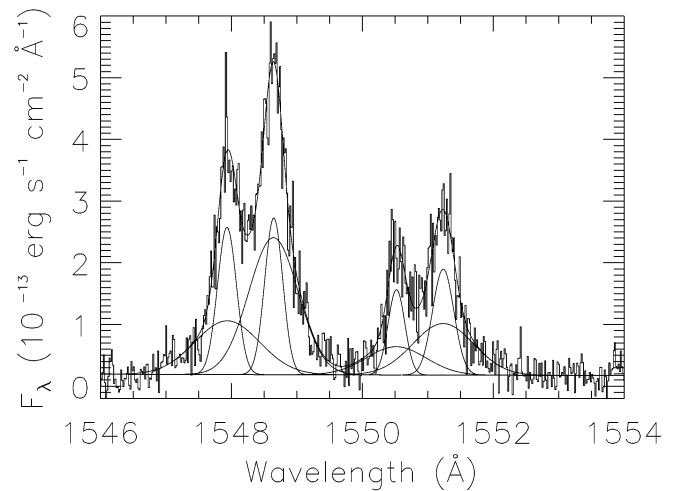


FIG. 11.—Two-Gaussian models for the C IV lines from phase 1905.95.

flux, unlike models for the K star component and other stars. Furthermore, considerable variability is observed in the relative strengths of the two components at other phases; at several phases the intensity of the G star narrow component is greater than that for the broad feature.

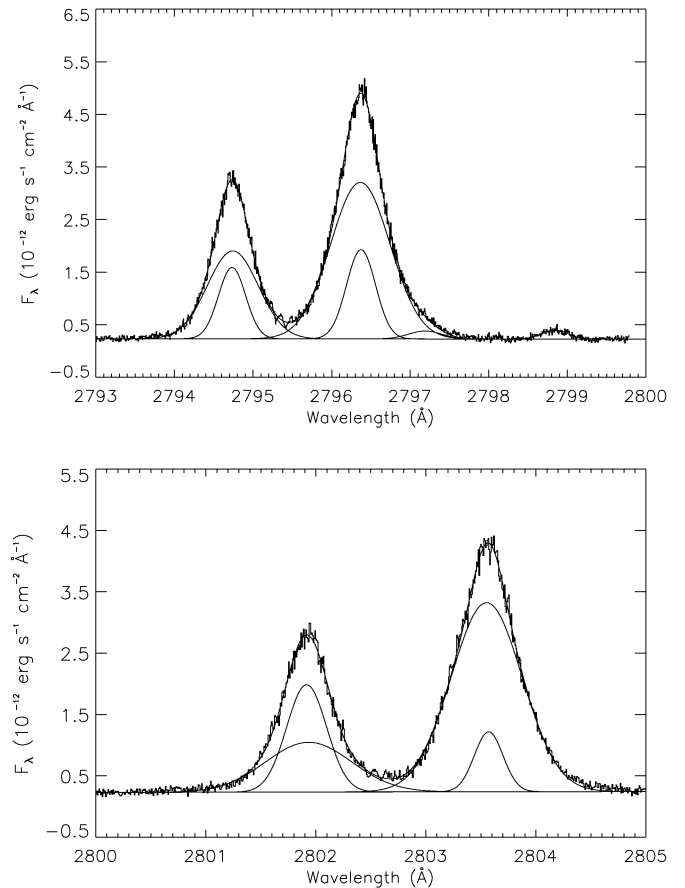


FIG. 12.—Two-Gaussian models for the Mg II *h* and *k* lines from quadrature phase 1905.96. Note that for simplicity, the interstellar absorption feature has been approximated by a single Gaussian and removed from the spectrum. The 2797.998 Å Mg II subordinate *k* line of the K star was fixed at the same peak intensity and width as observed at phase 1906.33, where it is unblended from the other lines but fixed with the predicted stellar radial velocity for phase 1905.96.

3.3.2. Anisotropic Models

Although reasonable fits to the C IV and Mg II may be obtained with multiple Gaussians, close inspection shows that the extended emission wings are still not fitted well. In the case of V824 Ara the wings are highly variable and could not be modeled with a constant Gaussian. To see whether we could improve the fit and perhaps obtain a model with a clear physical interpretation, we applied the anisotropic turbulence (AT) model presented by Gray (1992). This model was successfully applied to the O V profile in V711 Tau by Robinson et al. (1996). In the AT model, the line profile's non-Gaussian shape results from the relative contribution of a radial macroturbulent velocity distribution $[\Theta_R(V_R)]$ with fractional covering area A_R , and a tangential or horizontal distribution $[\Theta_T(V_T)]$ covering area A_T . The distributions are assumed to be Gaussian for a given $V_{R,T}$, while A_T is taken to be $1.0 - A_R$ for simplicity. The observed flux is then the standard convolution

$$F_\nu = \int I_\nu^o * [A_R \Theta_R(V_R) + A_T \Theta_T(V_T)] \cos \theta d\omega \quad (1)$$

integrated over the entire disk, where θ is the angle between the line of sight and the turbulent motion. The intrinsic line profile, I_ν^o , includes microturbulence (ξ), the rotational velocity ($v \sin i$), and linear limb brightening or darkening with coefficient ϵ . We accounted for the instrumental point-spread function, and we used the Marquardt method of χ^2 minimization. For each model, the central position (λ_{meas}), V_R , V_T , and peak intensity are free parameters for each profile. Although ξ could be varied as well, little improve-

ment is made in doing so. The results were only weakly dependent on ξ and ϵ , so we fixed these parameters at $\epsilon = -0.2$ and $\xi = 12 \text{ km s}^{-1}$.

A comparison between the two-Gaussian and AT models is shown in Figure 13. Although the radial component dominates the profile, the tangential contribution is needed to fit the extended wings. Both fits have χ^2 around 0.10 and are very similar in quality, although the wings are fitted slightly better in the AT model. Similar results were found for the Mg II k line. Figure 14 shows a representative AT fit to the C IV profile. Parameters of these fits are given in Table 10.

In either scheme—two-Gaussian or AT—modeling two stellar profiles as a function of phase is extremely challenging. In the case of AB Dor, the C IV modeling of Vilhu et al. (1998) was for a single star, where rotation dominates all other line-broadening processes, and they assumed the broad wings were constant. Because of their lower visibility, proper characterization of the extended wings requires that as much of their extent as possible be visible. Near conjunction up to half the line wing may be lost in the profile of the companion star, while at conjunction the wings represent a combination of flux from both stars. Both profiles are clearly variable, with fluctuations in the line core, as well as the wings. It is also clear that the representative AT fit shown in Figure 13 will not readily fit the Mg II lines at the other phases, because of variability in the total line flux and width. Mapping these variations as a function of rotational phase is beyond the scope of this paper.

Once we developed acceptable fits as described above, we attempted to fit all the other phases. In addition, we attempted to subtract the representative fits from the other

TABLE 10
ANISOTROPIC TURBULENCE MODEL

Comp.	λ_{meas} (Å)	ΔV^a (km s ⁻¹)	V_R (km s ⁻¹)	V_T (km s ⁻¹)	A_R	Flux (10 ⁻¹² ergs s ⁻¹ cm ⁻²)
V824 Ara C IV 1548 Å, $\phi = 1906.95$						
K0 V-IV	1547.857	18.0	86.8 ± 4.9	206.1 ± 18.5	0.86 ± 0.02	0.18
G5 IV	1548.770	25.8	54.3 ± 1.4	188.9 ± 6.9	0.83 ± 0.01	0.44
V824 Ara C IV 1550 Å, $\phi = 1906.95$						
K0 V-IV	1550.391	10.8	49.3 ± 3.4	2702 ± 472	0.96 ± 0.02	0.08
G5 IV	1551.349	26.9	19.2 ± 2.4	177.7 ± 8.4	0.70 ± 0.02	0.24
V824 Ara Mg II h Line, $\phi = 1906.96$						
K0 V-IV	2801.916	-2.9	33.6 ± 4.4	94.8 ± 11.8	0.80 ± 0.03	1.60
G5 IV	2803.558	-6.7	45.0 ± 3.2	95.0 ± 9.5	0.85 ± 0.02	2.89
V824 Ara Mg II k Line, $\phi = 1906.96$						
K0 V-IV	2794.734	-0.5	44.1 ± 3.3	75.9 ± 10.4	0.88 ± 0.02	1.89
G5 IV	2796.376	5.2 ^b	51.7 ± 2.2	129.3 ± 7.0	0.84 ± 0.01	3.79
V711 Tau Mg II h Line, $\phi = 0.73^\circ$						
K1 IV	2802.140	-4.6	100.2 ± 0.1	193.2 ± 0.5	0.98 ± 0.00	2.14
G5 IV	2803.180	5.7	29.4 ± 0.1	...	1.00 ± 0.00	0.17
V711 Tau Mg II k Line, $\phi = 0.73^\circ$						
K1 IV	2794.970	-3.9	118.0 ± 0.1	181.0 ± 0.2	0.98 ± 0.00	2.91
G5 IV	2795.920	-4.4	48.1 ± 0.1	...	1.00 ± 0.00	0.32

^a Radial velocity with respect to predicted orbital velocity.

^b Contaminated by the Mg II subordinate line at 2797.998 Å.

^c Here $\xi = 15.9 \text{ km s}^{-1}$, left as free parameter.

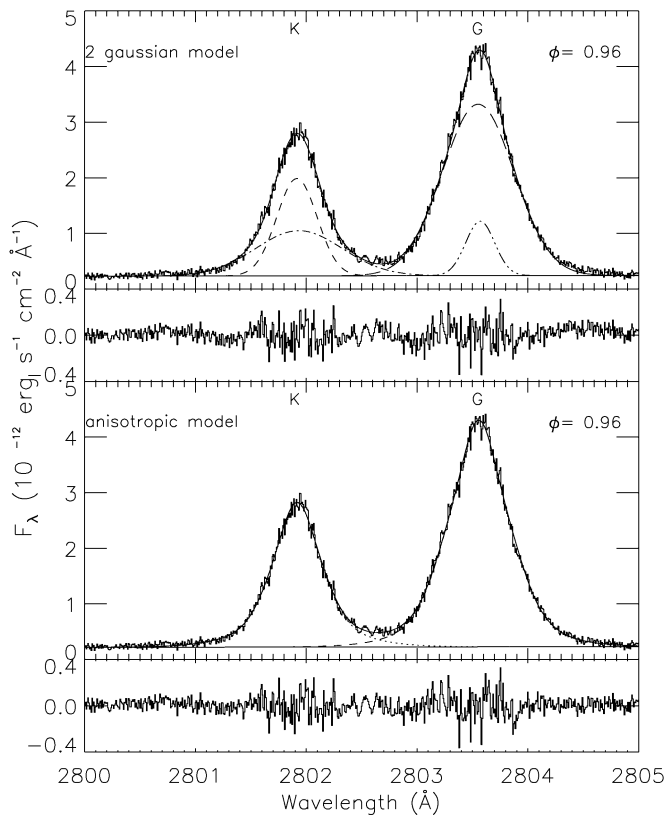


FIG. 13.—Comparison between the two-Gaussian and anisotropic turbulence model fits to the Mg II *h* lines, showing the broad and narrow Gaussian components for each star and the fit to the observed profile at phase 1906.96 (*top*) and the AT fit compared with the data (*bottom*). The difference between the model and the observed profile is shown below each fit.

phases after correcting for orbital velocity. However, profile blending and flares prevented us from applying these model fits consistently to all the observed phases. We are able only to conclude that the lines, fluxes and profiles were changing considerably during the period of our the observations.

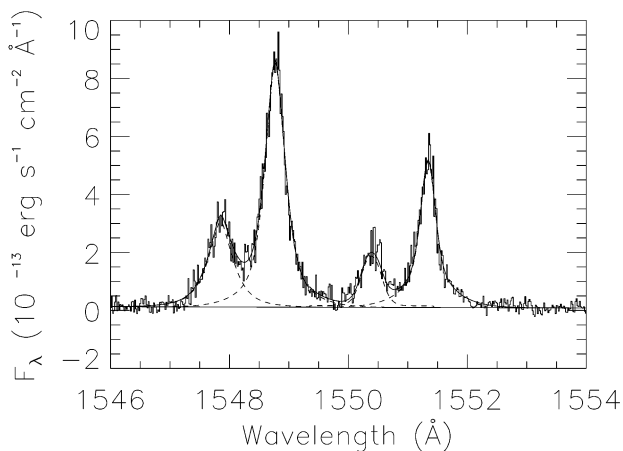


FIG. 14.—Anisotropic turbulence model fitted to C IV at phase 1906.95

4. CONCLUSIONS

We completed a multiwavelength observing campaign to study the short-period binary system V824 Ara throughout a single rotational cycle in 1996 May. We obtained over 48,000 spectra with the GHRS, and we arranged supporting observations in the radio (ATCA), extreme ultraviolet (*EUVE*), and the visual (spectroscopy from CTIO and photometry from several southern sites). In this paper, we present results derived from our ultraviolet, EUV, and radio data.

We analyzed several flares that were observed simultaneously at several wavelengths. We identified and measured all the UV and EUV emission line fluxes. High-resolution spectra with GHRS allowed us to study the detailed shape of the emission-line profiles as well. We demonstrate that the profiles are not well fitted by single Gaussian components. Like other active stars observed with GHRS, the profiles show extended and often asymmetric line wings. We offer two alternative interpretations of these extended wings.

With only one full rotation covered by the *HST* observations, combined with at least one flare and indications of a large degree of variability (especially in the radio data), we cannot uniquely determine the spatial relation between the spots observed in visible-band photometry and Doppler images with the structure of active regions higher in the atmosphere. We nevertheless were able to compare the probable location of flaring regions with the location of starspots. Since the Strassmeier & Rice (2000) optical maps show the presence of polar spots, correlating flares observed at different phases with features on the stars is difficult. The strongest evidence for a flare in the UV and X-ray data occurs around phase 1906.6. This corresponds to the maximum spot visibility of the G star, but the velocity of the flaring emission is closer to that of the secondary. A velocity shift due to the motion of the flaring material cannot be ruled out. The presence of radio flares at several phases may indicate that the active flaring regions are fairly well distributed over the star and not directly connected to the spots or may be related to one or both star's polar features that are always visible.

Flaring and non-phase-dependent variability complicate any systematic attempt to understand the line profiles. While we have had some success at using simple Gaussian and AT models, no model fits the lines perfectly at all phases. Additional models, perhaps including hydrodynamic flare motions, will need to be developed.

Support for this work was provided by STScI grant GO-06072.01-94A and by NASA *EUVE* grant S-57788-Z. We are deeply indebted to the other observers who participated in this campaign: A. Brown, E. Budding, J.-F. Donati, D. Downing, D. Inwood, I. Jordan, D. Kilkenny, F. Marang, R. Osten, O. Petterson, K. Strassmeier, S. Walker, and F. Walter. We thank V. Airapetian, R. Robinson, K. Strassmeier, J. Valenti, and B. Wood for helpful comments and/or software.

REFERENCES

- Bevington, P. R., & Robinson, D. K. 1992, *Data Reduction and Error Analysis for the Physical Sciences* (New York: McGraw-Hill), 161
- Blackwell, J., Shore, S. N., Robinson, R. D., Feggans, K., Lindler, D., Malumuth, E., Sandoval, J., & Ake, T. B. 1993, *A User's Guide to the GHRS Software (Version 2.1; Baltimore: STScI)*
- Collier-Cameron, A. 1995, *MNRAS*, 275, 534
- Cutispoto, G. 1993, *A&AS*, 102, 655
- Dempsey, R. C., Linsky, J. L., Schmitt, J. H. M. M., & Fleming, T. A. 1993a, *ApJS*, 86, 599
- . 1993b, *ApJ*, 413, 333
- Dempsey, R. C., et al. 1998, in *ASP Conf. Ser. 154, Cool Stars, Stellar Systems, and the Sun*, ed. R. A. Donahue & J. A. Bookbinder (San Francisco: ASP), 1402
- Dempsey, R. C., Neff, J. E., Thorpe, M. J., Linsky, J. L., Brown, A., Cutispoto, G., & Rodonò, M. 1996, *ApJ*, 470, 1172
- Donati, J.-F., Brown, S. F., Semel, M., Rees, D. E., Dempsey, R. C., Matthews, J. M., Henry, G. W., & Hall, D. S. 1992, *A&A*, 265, 682
- Gray, D. 1992, *The Observation and Analysis of Stellar Photospheres* (New York: Cambridge Univ. Press), 407
- Güdel, M., Schmitt, J. H. M. M., Benz, A. O., & Elias, N. M., II. 1995, *A&A*, 301, 201
- Hatzes, A. P., & Kürster, M. 1999, *A&A*, 346, 432
- Heap, S. R., et al. 1995, *PASP*, 107, 871
- Joncour, I., Bertout, C., & Bouvier, J. 1994, *A&A*, 291, L19
- Lim, J., Nelson, G. J., Castro, C., Kilkenny, D., & van Wyk, F. 1992, *ApJ*, 388, L27
- Lim, J., White, S. M., Nelson, G. J., & Benz, A. O. 1994, *ApJ*, 430, 332
- Lindler, D. J. 1995, in *Calibrating the Hubble Space Telescope: Post Servicing Mission*, ed. A. Koratkar & C. Leitherer (Baltimore: STScI), 216
- Linsky, J. L., & Wood, B. E. 1994, *ApJ*, 430, 342
- Linsky, J. L., Wood, B. E., Judge, P., Brown, A., Andrulis, A., & Ayres, T. 1995, *ApJ*, 442, 381
- Maran, S. P., et al. 1994, *ApJ*, 421, 800
- Neff, J. E., Pagano, I., Rodonò, M., Brown, A., Dempsey, R. C., Fox, D., & Linsky, J. L. 1996, *A&A*, 310, 173
- Neff, J. E., Walter, F. M., Rodonò, M., & Linsky, J. L. 1989, *A&A*, 215, 79
- Osten, R. A., & Brown, A. 1999, *ApJ*, 515, 746
- Pasquini, L., Cutispoto, G., Gratton, R., & Mayor, M. 1991, *A&A*, 248, 72
- Rice, J. B., & Strassmeier, K. G. 1996, *A&A*, 316, 164
- Robinson, R. D., Airapetian, V. S., Carpenter, K. G., & Maran S. P. 1996, *ApJ*, 469, 872
- Schultz, A. B., & Bacinski, J. 1996, *GHRS Instrument Science Report 78* (Baltimore: STScI)
- Soderblom, D. S., Eisenhamer, J., Hulbert, S., Leitherer, C., McGrath, M., Sherbert, L., & Skapik, J. 1996, *GHRS Instrument Science Report 73* (Baltimore: STScI)
- Soderblom, D. S., Sherbert, L. E., & Hulbert, S. J. 1993, in *Calibrating the Hubble Telescope*, ed. J. C. Blades & S. J. Osmer (Baltimore: STScI), 264
- Strassmeier, K. G., Hall, D. S., Fekel, F. C., & Scheck, M. 1993, *A&AS*, 100, 173
- Strassmeier, K. G., & Rice, J. B. 1998, *A&A*, 330, 685
- . 2000, *A&A*, 360, 1019
- Strassmeier, K. G., et al. 1991, *A&A*, 247, 130
- Vilhu, O., Muhli, P., Huovelin, J., Hakala, P., Rucinski, S. M., & Collier-Cameron, A. 1998, *AJ*, 115, 1610
- Vogt, S. S., Hatzes, A. P., Kürster, M., & Misch, A. A. 1999, *ApJS*, 121, 547
- Walter, F. M., Neff, J. E., Gibson, D. M., Linsky, J. L., Rodonò, M., Gary, D. E., & Butler, C. J. 1987, *A&A*, 186, 241
- White, S. M., Kundu, M. R., & Jackson, P. D. 1989, *A&A*, 225, 112
- Wood, B. E., Harper, G. M., Linsky, J. L., & Dempsey, R. C. 1996, *ApJ*, 458, 761
- Wood, B. E., & Linsky, J. L. 1998, *ApJ*, 492, 788
- Wood, B. E., Linsky, J. L., & Ayres, T. R. 1997, *ApJ*, 478, 745